

Article

Corrosion Resistance and Conductivity of Ta-Nb-N-Coated 316L Stainless Steel as Bipolar Plates for Proton Exchange Membrane Fuel Cells

Qizhong Li ^{1,2,3}, Chuan Ding ^{1,2}, Mai Yang ¹, Meijun Yang ^{1,4}, Tenghua Gao ^{1,4}, Song Zhang ^{1,2,4}, Baifeng Ji ^{1,5} , Takashi Goto ^{1,2} and Rong Tu ^{1,2,4,*} 

¹ Chaozhou Branch of Chemistry and Chemical Engineering Guangdong Laboratory, Chaozhou 521000, China; qizhongli@whut.edu.cn (Q.L.); dingchuan@whut.edu.cn (C.D.); 245954@whut.edu.cn (M.Y.); liyangmeijun@163.com (M.Y.); gao@appi.keio.ac.jp (T.G.); kobe@whut.edu.cn (S.Z.); jbfeng@whut.edu.cn (B.J.); takashi_goto@outlook.jp (T.G.)

² State Key Laboratory of Advanced Technology for Materials Synthesis and Processing, Wuhan University of Technology, Wuhan 430070, China

³ Hubei Key Laboratory of Advanced Technology for Automotive Components, Wuhan University of Technology, Wuhan 430070, China

⁴ Hubei Technology Innovation Center for Advanced Composites, Wuhan University of Technology, Wuhan 430070, China

⁵ School of Civil Engineering and Architecture, Wuhan University of Technology, 122 Luoshi Road, Wuhan 430070, China

* Correspondence: turong@whut.edu.cn

Abstract: The large-scale application of stainless steel (SS) bipolar plates (BPs) in proton exchange membrane fuel cells (PEMFCs) is mainly limited by insufficient corrosion resistance and electrical conductivity. In this work, Ta-Nb-N coatings were prepared on 316L SS substrates by unbalanced magnetron sputtering to improve corrosion resistance and conductivity. The Ta-Nb-N coatings had a dense structure without obvious defects. In simulated PEMFC cathode environments consisting of 0.5 M H₂SO₄ + 2 ppm HF at 70 ± 0.5 °C, which is harsher than the U.S. Department of Energy specification, the corrosion current density of Ta-Nb-N-coated BPs was reduced to $2.2 \times 10^{-2} \mu\text{A}\cdot\text{cm}^{-2}$. Ta-Nb-N-coated samples showed better electrical conductivity than 316L SS, which had an excellent interfacial contact resistance of 9.2 mΩ·cm². In addition, the Ta-Nb-N-coated samples had a water contact angle of 100.7°, showing good hydrophobicity for water management. These results indicate that Ta-Nb-N coatings could be a promising material for BPs.

Keywords: PEMFCs; bipolar plates; Ta-Nb-N coating; corrosion resistance; interfacial contact resistance



Citation: Li, Q.; Ding, C.; Yang, M.; Yang, M.; Gao, T.; Zhang, S.; Ji, B.; Goto, T.; Tu, R. Corrosion Resistance and Conductivity of Ta-Nb-N-Coated 316L Stainless Steel as Bipolar Plates for Proton Exchange Membrane Fuel Cells. *Coatings* **2024**, *14*, 542. <https://doi.org/10.3390/coatings14050542>

Academic Editor: Frederic Sanchette

Received: 7 April 2024

Revised: 18 April 2024

Accepted: 22 April 2024

Published: 26 April 2024



Copyright: © 2024 by the authors. Licensee MDPI, Basel, Switzerland. This article is an open access article distributed under the terms and conditions of the Creative Commons Attribution (CC BY) license (<https://creativecommons.org/licenses/by/4.0/>).

1. Introduction

Proton exchange membrane fuel cells (PEMFCs) are one of the current hotspots in the field of hydrogen energy research, with advantages such as high efficiency, zero pollution, and high reliability [1–3]. As key components of PEMFCs, bipolar plates (BPs) are responsible for functions such as collecting and conducting current, separating oxidants and reductants, and managing water and heat [4,5]. Therefore, BPs are required to have good thermal and electrical conductivity, high corrosion resistance, excellent mechanical properties, and low cost [6,7]. Traditionally, the BPs of PEMFCs are typically made of graphite, renowned for its excellent chemical stability and conductivity [8–10]. However, the inherent low mechanical strength of graphite poses a challenge in reducing the thickness of the graphite BPs, resulting in a large volume and weight of the fuel cell stack [11,12]. Stainless steel (SS) is considered a substitute for graphite due to its high electrical conductivity, excellent mechanical properties, and machinability to be thin foils [13]. Nevertheless, stainless steel faces significant corrosion and passivation challenges when exposed to acidic,

hot, and humid conditions in the case of PEMFCs. This corrosion not only increases the interfacial contact resistance (ICR) but also contributes to poisoning of the membrane electrode assembly (MEA), ultimately reducing the efficiency of the fuel cell [14,15]. Hence, a conductive coating with high corrosion resistance is essential to facilitate the application of SS in metallic BPs [16].

The transition metal Ta and its nitrides are considered promising coating candidates due to their exceptional combination of corrosion resistance and electrical conductivity [17,18]. Ta and its nitride coatings are commonly prepared by physical vapor deposition (PVD), which has the advantages of high film purity, accurate control, and fast deposition rate. Choe et al. [19] deposited TaN_x films on 316L SS by magnetron sputtering, and the corrosion resistance of TaN_x -coated samples was better than that of 316L SS. However, like most coatings, the films have obvious columnar structures that can become channels for corrosive fluids to penetrate the coating, causing severe localized corrosion [20,21]. To reduce the influence of columnar structures, poly-component metallic compound coatings have been widely studied because the introduction of suitable elements can inhibit the growth of columnar crystals by changing the crystal structure and growth direction of the material during film growth [21–23]. For example, Bi et al. [24] produced CrN coatings doped with different Al contents by magnetron sputtering, in which the reduction in the CrN grain size led to a more positive corrosion potential and lower corrosion current density of the Cr-Al-N films. However, the corrosion current density of the Cr-Al-N films was higher than the U.S. Department of Energy (DOE) standard at an operating potential of 0.6 V. Peng et al. [25] produced TiSiN coatings on a Ti-6Al-4V substrate, showing good electrochemical stability by adding Si to the TiN coatings and reducing the contact resistance to $14.7 \text{ m}\Omega\cdot\text{cm}^2$. Jin et al. [26] prepared TiCN coatings with varying C contents on 316L SS using closed-field unbalanced magnetron sputter ion plating. They found that the addition of C to the TiN coating inhibited the growth tendency of the typical columnar crystalline structure of TiN, resulting in a smoother and denser surface. TiCN-coated samples showed improved corrosion resistance and electrical conductivity compared to TiN-coated samples.

At present, there is a lack of reports on the Ta-based poly-component coatings applied in the coatings of BPs in PEMFCs. Not only does Nb offer excellent corrosion resistance and electrical conductivity, but it also exhibits good compatibility with Ta, making Nb a favorable option for Ta-based poly-component coatings [27,28]. We expect the ternary Ta-Nb-N coatings can inhibit the growth of columnar crystals, ultimately achieving a dense structure with fewer corrosion pathways. Here, Ta-Nb-N coatings were prepared on a 316L SS surface by unbalanced magnetron sputtering. The phase, morphology, corrosion resistance, and ICR of Ta-Nb-N coatings prepared under different pressures were investigated.

2. Materials and Methods

2.1. Deposition of Coatings

Figure 1 shows a schematic of the magnetron sputtering apparatus used in this work. The plasma bombarded the targets under the control of a magnetic field, sputtering the target atoms, which reacted with nitrogen during sputtering or deposition to form nitride coatings. Ta and Nb, with a purity of 99.95%, were selected as the targets. 316L SS and monocrystalline silicon (100) were used as substrates. The dimensions of the 316L SS substrates were $60 \text{ mm} \times 60 \text{ mm} \times 2 \text{ mm}$. The 316L SS substrates were polished by diamond suspensions and washed in acetone, ethanol, and distilled water by sonication for 10 min each, followed by drying with nitrogen gas. The chamber was first evacuated to $5 \times 10^{-4} \text{ Pa}$; then, Ar was introduced; and the chamber pressure stabilized at 8 Pa. The substrates were cleaned by glow discharge under the bias of -800 V for 15 min. The internal pressure of the chamber was maintained at 0.5 to 2 Pa by injecting 10 mL/min of Ar and 2 mL/min of N_2 after lowering the substrate bias to -100 V . Deposition was carried out for 30 min with the power of 50 W for the Ta and Nb targets. The specimens deposited under the pressure of 0.5, 1, 1.5, and 2 Pa are named TaNbN-0.5, TaNbN-1.0, TaNbN-1.5, and TaNbN-2.0, respectively.

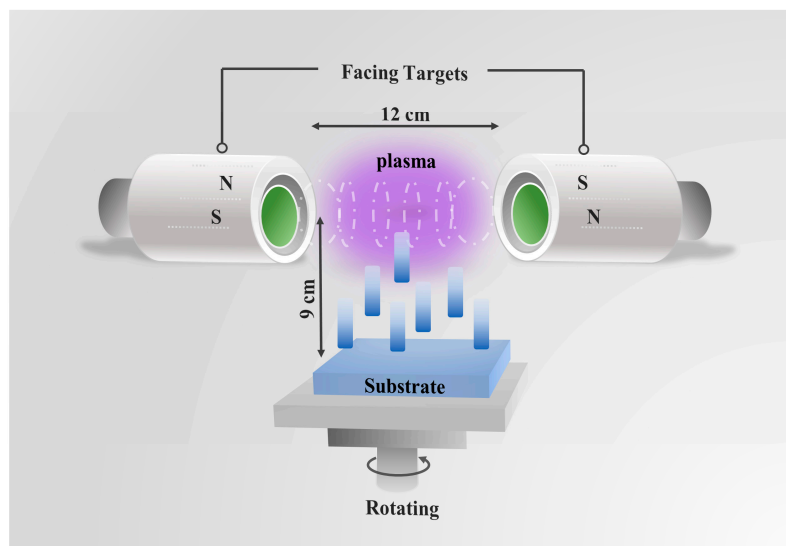


Figure 1. Schematic illustration of the technique used for this work.

2.2. Material Characterizations

The phase composition of the Ta-Nb-N coatings was determined using grazing incidence X-ray diffraction (XRD, Empyrean, Panalytical, Malvern, UK) at 0.5° incident angle with Cu-K α radiation. The chemical composition of the Ta-Nb-N coatings was analyzed using an X-ray photoelectron spectrometer (XPS, AXIS SUPRA, Kratos, Manchester, UK). The surface and cross-sectional morphology and composition of the coatings were characterized using a field emission scanning electron microscope (SEM, GeminiSEM 300, Carl Zeiss, Jena, Germany) equipped with energy dispersive spectroscopy (EDX). The surface roughness of coatings was evaluated by using an atomic force microscope (AFM, Dimension Icon, Bruker, Karlsruhe, Germany).

2.3. Electrochemical Measurements

A three-electrode electrochemical cell system was set up to perform electrochemical experiments (Figure S1), consisting of a sample (working electrode), a saturated calomel electrode (reference electrode, SCE), and a platinum sheet electrode (counter electrode). To accelerate the reaction, we selected a 0.5 M H₂SO₄ + 2 ppm HF solution with a temperature of $70 \pm 0.5^\circ\text{C}$ as the corrosion solution instead of the U.S. DOE protocol (0.5 mM H₂SO₄ + 0.1 ppm HF at 80°C) [29]. Before testing, we conducted an open circuit potential (OCP) test on the samples for 1 h to ensure a stable state. Under OCP, Electrochemical impedance spectroscopy (EIS) testing was conducted in the frequency range of 100 kHz to 0.01 Hz with a disturbance voltage of 10 mV, and equivalent circuit fitting was performed. To simulate the cathode environment of PEMFCs for polarization testing, air was injected into the etching solution. The corrosion of the samples was evaluated at each potential using a scanning speed of 1 mV/s for the potentiodynamic polarization testing, within the range of $-0.4 \text{ V}_{\text{SCE}}$ to $1.0 \text{ V}_{\text{SCE}}$. To evaluate the long-term durability of the coatings, a potentiostatic polarization test was performed for 6 h at an applied voltage of $0.6 \text{ V}_{\text{SCE}}$. The concentration of dissolved elements in the electrolyte was measured using inductively coupled plasma-atomic emission spectroscopy (ICP-AES).

2.4. Interfacial Contact Resistance (ICR) and Water Contact Angle Measurements

The ICR was tested using Wang's method [30]. The samples were sandwiched between two sheets of conductive carbon paper (Toray TGP-H-090, Toray, Tokyo, Japan) and placed between two gold-plated copper plates (Figure S2). The resistance was measured using an ohmmeter while a pressure of 1.4 MPa was applied to both sides of the gold-plated copper plate. The specific calculation method of the ICR can be found in the literature [31]. To

evaluate the hydrophobicity of the coatings, we tested the water contact angle of 316L SS and the coated samples at room temperature (25°C) using a contact angle tester (DSA100, Kruss, Hamburg, Germany).

3. Results

3.1. Phase Structure

The XRD spectra of the Ta-Nb-N coatings are shown in Figure 2, with four peaks near 35.5° , 41.2° , 60.1° , and 71.9° at 2θ , which is associated with (111), (200), (220), and (311) crystal planes of cubic TaN (JCPDS #49-1283) or cubic NbN (JCPDS #38-1155), respectively. The diffraction peak intensity of the TaNbN-0.5 coating was low, which may be due to poor crystallinity. As shown in Figure 2b, the diffraction angles of TaNbN-1.0, TaNbN-1.5, and TaNbN-2.0 coatings are between those of cubic TaN and cubic NbN, attributing to the close similarity in lattice parameters between cubic TaN and cubic NbN, resulting in the formation of a solid solution [32].

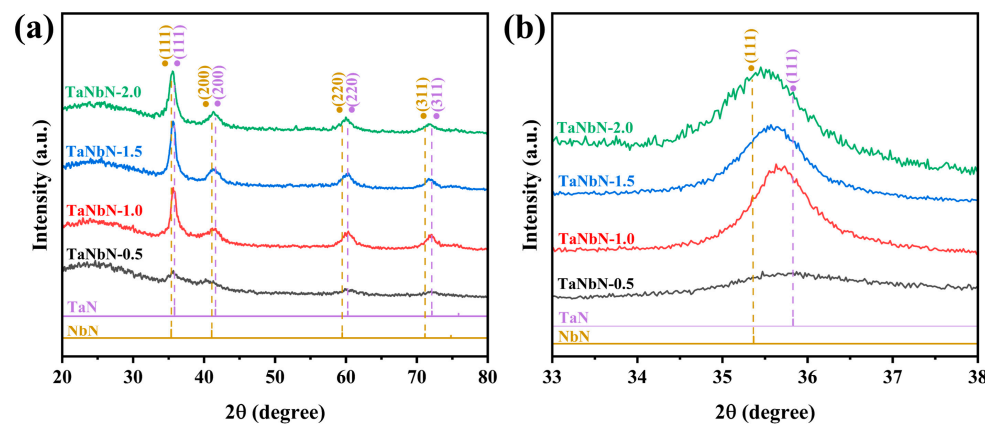


Figure 2. XRD spectrum of Ta-Nb-N coatings: (a) full spectrum and (b) partial spectrum.

XPS was used to analyze the surface state of the Ta-Nb-N coatings prepared at each deposition pressure. Figure 3a shows the XPS spectra for Ta 4f. The peaks at 23.4 eV and 25.1 eV are associated with Ta-N, while the peaks at 25.7 eV and 27.6 eV are associated with Ta-O [33]. Figure 3b shows the XPS spectra for Nb 3d. The 203.6 eV lower binding energy is interpreted as Nb-N, while the 206.8 eV higher binding energy was identified as Nb-O [34,35]. Furthermore, the peaks at 204.6 eV are associated with the NbN_xO_y compound [23]. The presence of oxygen was due to oxidation of the sample surface during storage and transfer in the air environment [36].

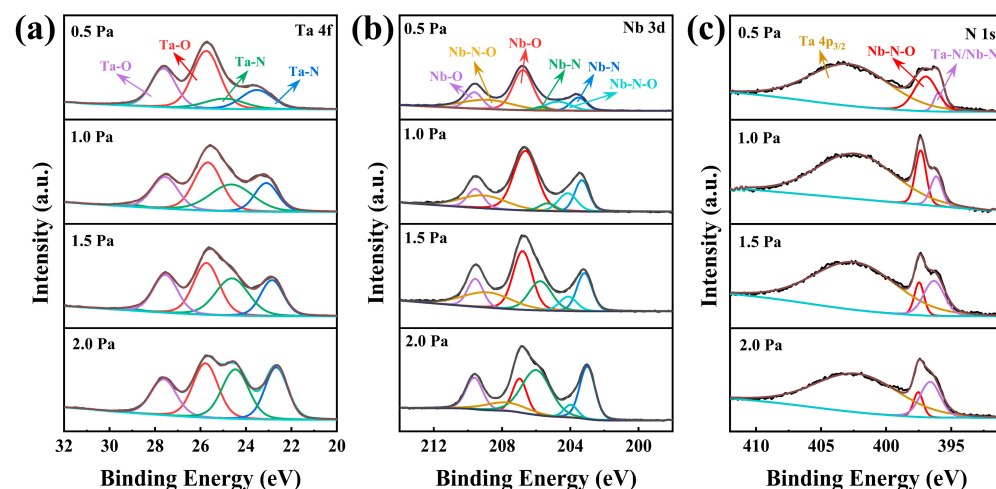


Figure 3. XPS spectra of the Ta-Nb-N coatings (a–c).

3.2. Surface Morphology

The SEM surface morphology of the Ta-Nb-N coatings is shown in Figure 4a–d. As the deposition pressure increased from 0.5 Pa to 2.0 Pa, the grain size of the coating became larger, and the surface became rougher. Figure 4e–h shows the SEM cross-sectional morphology of the Ta-Nb-N coatings. All Ta-Nb-N coatings were dense, without microcracks or voids, which can effectively prevent the penetration of corrosive fluids. The coating thickness increased with increasing deposition pressure. As shown in Figure 4i–l, the EDS elemental mappings demonstrate a homogeneous distribution of Ta, Nb, and N over the surface. The elemental compositions can be seen in Table 1; the composition of metal (Ta and Nb) versus N was close to 1. Figure 5 shows the AFM topography of each coating, revealing distinct surface features. As the deposition pressure increased, the root-mean-square roughness of the coatings exhibited a progressive rise, measuring 0.70, 3.16, 3.38, and 3.56 nm, respectively. The smooth and uniform surface can help to improve corrosion resistance and increase the contact Angle of the coating. The coating produced at 0.5 Pa was the thinnest and smoothest because the deposition pressure was low, resulting in a reduced probability of collisions between metallic and non-metallic particles [24]. As a result, since the sputtered particles had higher energy when they hit the substrate, and under the impact of the high energy, the relatively thinnest and smoothest coating was formed [37].

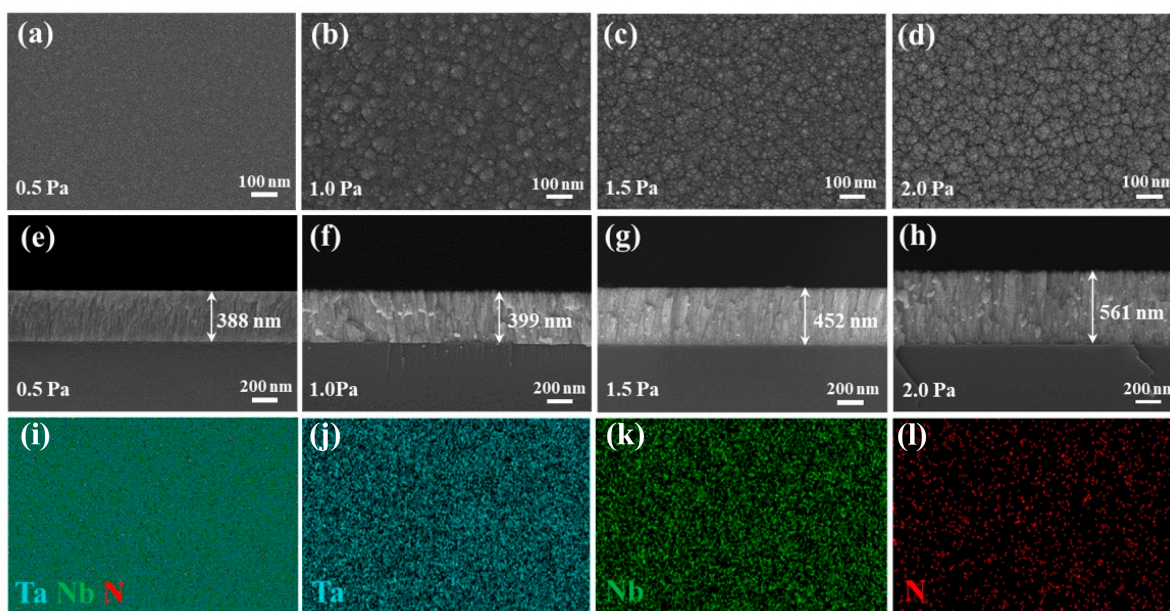


Figure 4. SEM surface (a–d) and cross-sectional (e–h) morphologies of TaNbN-0.5, TaNbN-1.0, TaNbN-1.5, and TaNbN-2.0 coatings. EDS elemental mappings (i–l) of TaNbN-0.5 coating.

Table 1. Element contents of Ta-Nb-N coatings.

Samples	Ta (at. %)	Nb (at. %)	N (at. %)
TaNbN-0.5	26.74	16.39	56.88
TaNbN-1.0	29.26	19.78	50.96
TaNbN-1.5	28.91	19.47	51.62
TaNbN-2.0	28.29	15.10	56.61

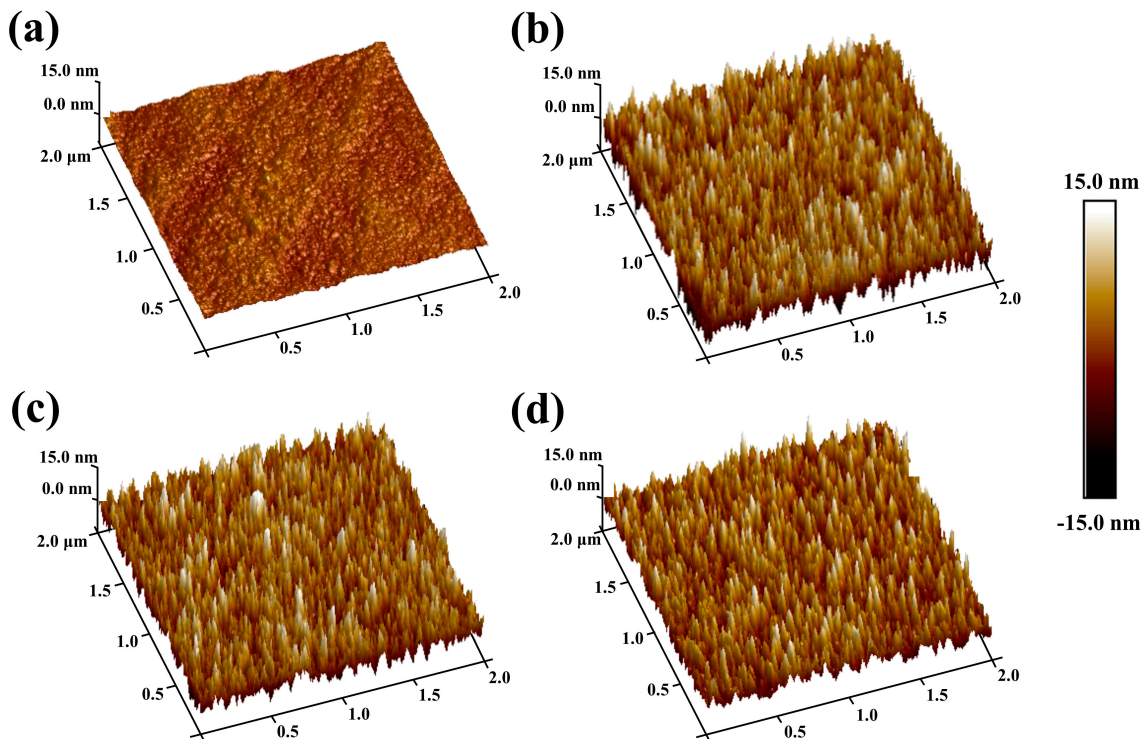


Figure 5. AFM surface topography of (a) TaNbN-0.5, (b) TaNbN-1.0, (c) TaNbN-1.5, and (d) TaNbN-2.0 coatings.

3.3. Electrochemical Test

Figure 6 shows the potentiodynamic polarization test curve of different coatings and 316L SS. Under the same applied voltage, the corrosion current density of all coated samples was lower than that of 316L SS. In addition, 316L SS showed an active-passive region in the anode region and then entered the steady passive region [38], whereas there was no active-passive region in the coated samples, indicating that the coatings had higher thermodynamic stability and chemical inertness [39]. Table 2 shows the fitting results of the potentiodynamic polarization curve. The corrosion current density of all coated samples was less than $1 \mu\text{A}\cdot\text{cm}^{-2}$, which meets the DOE standard [40]. At the cathode operating voltage of $0.6 \text{ V}_{\text{SCE}}$, the corrosion current density of the TaNbN-0.5-coated sample was $0.25 \mu\text{A}\cdot\text{cm}^{-2}$, which was much lower than that of 316L SS.

Figure 7 shows the corrosion current of coatings and 316L SS. The corrosion current density of each coating and 316L SS decreased rapidly due to the formation of a passivation film and then remained at a low value [26]. There were some peaks in the curve for 316L SS due to the destruction and regeneration of the passivation film. The corrosion current density of 316L SS was finally about $1.85 \times 10^{-6} \text{ A}\cdot\text{cm}^{-2}$, which was significantly higher than that of the coatings. The corrosion current density of all coatings was stable for 18 ks, indicating that Ta-Nb-N coatings can effectively resist corrosion in the simulating cathode working environment of PEMFCs. The corrosion current density of TaNbN-0.5 was $1.2 \times 10^{-8} \text{ A}\cdot\text{cm}^{-2}$, which can effectively protect the substrate. Following the potentiostatic polarization test, SEM tests were conducted on the coating samples. As illustrated in Figure 8, the surface of each coating sample appeared relatively intact, although a small number of defects were observed. This may be attributed to the presence of pits or dust on the substrate surface, which led to localized detachment of the coatings and the formation of holes during the potentiostatic polarization test. Furthermore, the edges of the holes are preferentially corroded, leading to the enlargement of the defects.

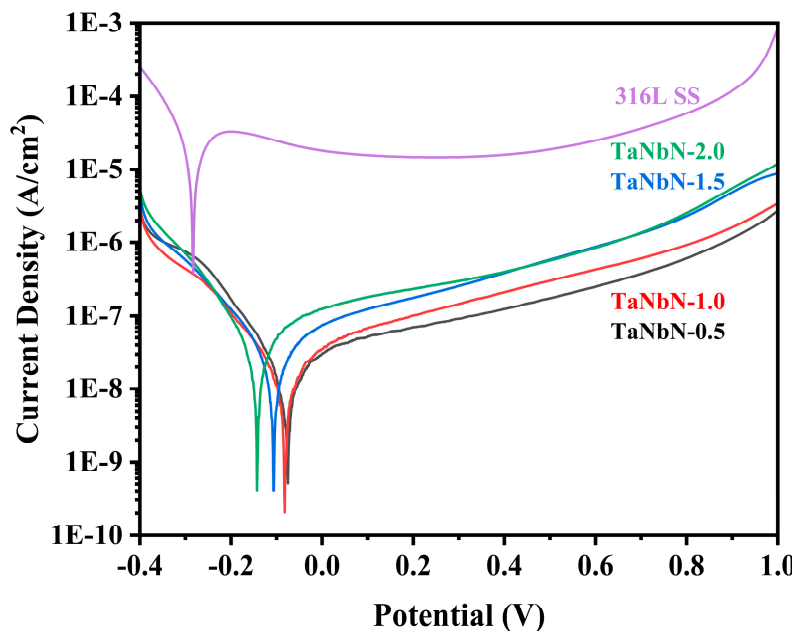


Figure 6. Potentiodynamic polarization curves of Ta-Nb-N coatings and 316L SS in the simulated PEMFCs cathode environment.

Table 2. Electrochemical parameters of Ta-Nb-N coatings and 316L SS in the simulated PEMFC cathode environment.

Samples	OCP	E_{corr}/V	$I_{corr}/\mu A \cdot cm^{-2}$	$I_{0.6V}/\mu A \cdot cm^{-2}$
316L SS	-0.185	-0.283	41.9	26.46
TaNbN-0.5	0.031	-0.075	0.022	0.25
TaNbN-1.0	0.028	-0.082	0.023	0.43
TaNbN-1.5	0.006	-0.107	0.035	0.86
TaNbN-2.0	0.005	-0.143	0.043	0.83

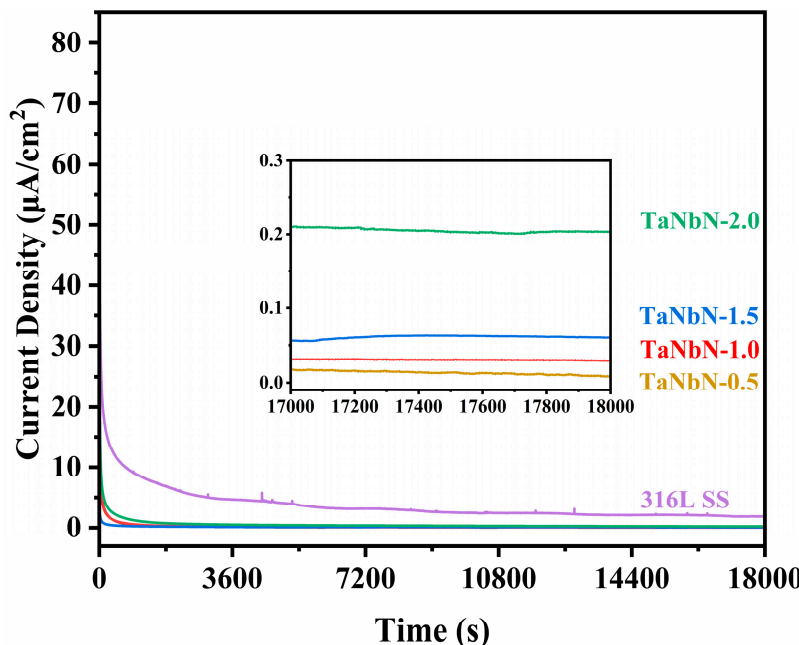


Figure 7. Potentiostatic polarization curves of Ta-Nb-N coatings and 316L SS in the simulated PEMFCs cathode environment at $0.6 V_{SCE}$.

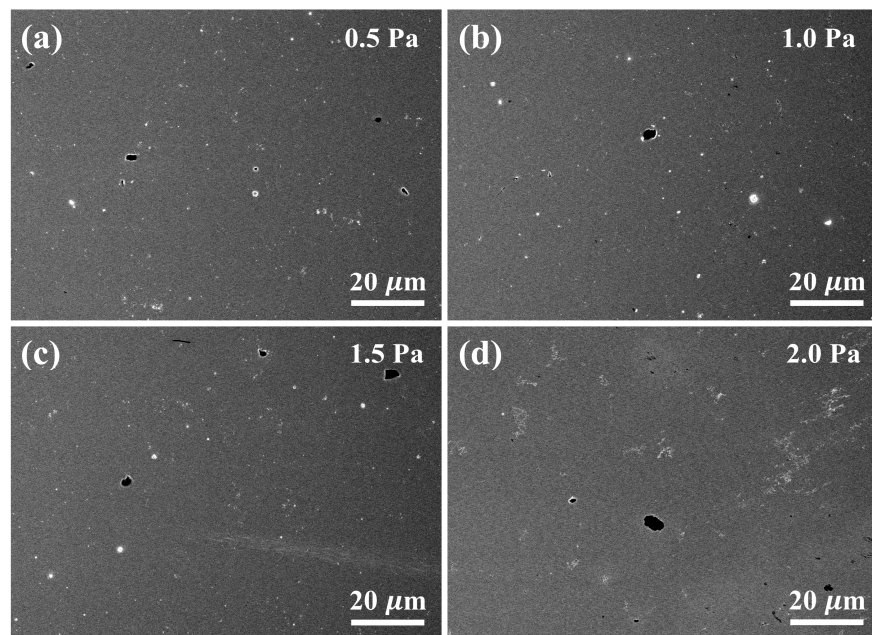


Figure 8. SEM surface morphologies of (a) TaNbN-0.5, (b) TaNbN-1.0, (c) TaNbN-1.5, and (d) TaNbN-2.0 coatings after potentiostatic polarization test.

In PEMFCs, metal cations generated by anodic corrosion of metal BPs enter the solution and migrate to the proton exchange membrane, causing poisoning of the MEA. Therefore, it is important to test the concentration of metal ions released in a simulated PEMFC environment. The corrosive liquid was removed after an 18 ks potentiostatic polarization test and analyzed by ICP-AES. As shown in Table 3, the 316L SS substrate exhibited a significantly higher release of metal ions compared to the coated samples, in particular, releasing significant amounts of Fe and Cr ions. Conversely, each coating shows a low concentration of released metal cations, effectively mitigating the potential impact on PEMFCs. This highlights the effectiveness of Ta-Nb-N coatings in providing robust protection to 316L SS, which may be attributed to the formation of dense and stable Ta-O-N and Nb-O-N passivation layers on the coating surface.

Table 3. ICP-AES results of Ta-Nb-N coatings and 316L SS.

Samples	Fe/ppm	Cr/ppm	Ni/ppm	Ta/ppm	Nb/ppm	Total/ppm
316L SS	9.3	1.53	0.37	-	-	11.2
TaNbN-0.5	-	-	-	0.15	0.41	0.56
TaNbN-1.0	-	-	-	0.21	0.43	0.64
TaNbN-1.5	-	-	-	0.25	0.51	0.76
TaNbN-2.0	-	-	-	0.27	0.52	0.79

Figure 9 shows the EIS diagrams of Ta-Nb-N coatings and 316L SS. In the Nyquist plot of Figure 9a, a larger semicircle diameter implies greater charge transfer resistance and greater corrosion resistance [41]. The semicircle diameter of the Ta-Nb-N coatings was significantly higher than that of 316L SS, indicating that the corrosion resistance was enhanced. In the Bode diagram of Figure 9b,c, the value of $|Z|$ in the low-frequency region can generally be used to analyze the corrosion resistance [26]. The 316L SS substrate showed two time constants because the passivation layer was partially destroyed in a strong corrosive environment, and the electrolyte passed through the damaged area, partially in direct contact with the substrate [42]. Log $|Z|$ vs. log F plot had a slope close to -1 in the frequency range from 0.01 Hz to 100 Hz, indicating that the Ta-Nb-N coatings had high chemical stability. According to the analysis of $|Z|$ at 10 mHz, the TaNbN-0.5 coating had the highest impedance and the best corrosion resistance.

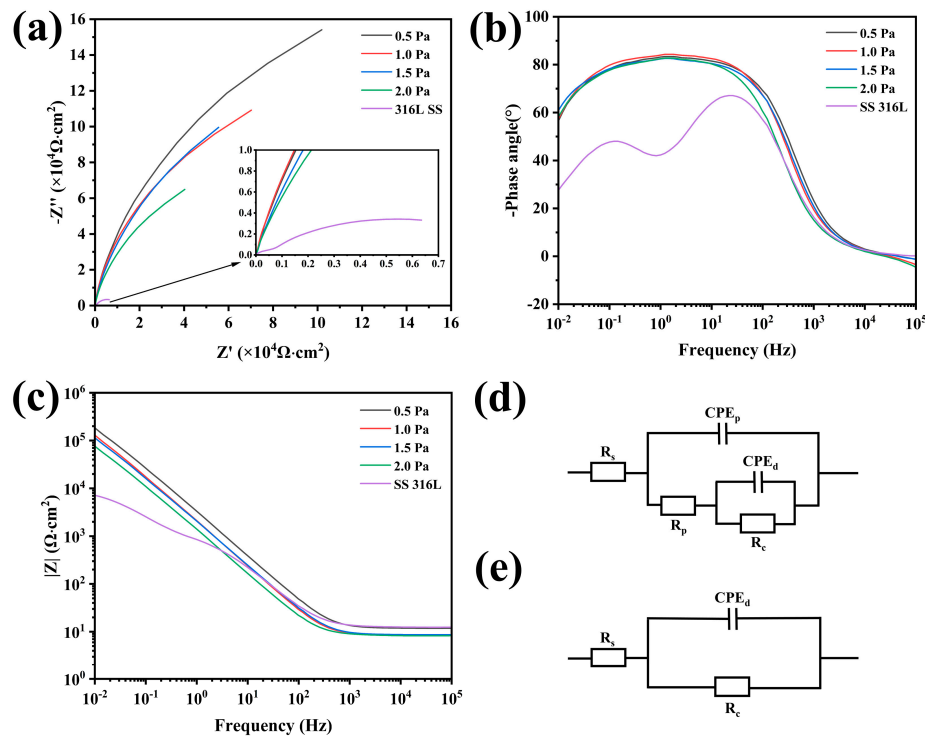


Figure 9. EIS results of 316L SS and Ta-Nb-N coatings: (a) Nyquist plots, (b,c) Bode plots, (d) equivalent circuit for 316L SS, and (e) equivalent circuit Ta-Nb-N coatings.

ZSimpWin 3.3 software was used to perform the fitting analysis of the EIS measurement data. Since 316L SS had two time constants, an equivalent circuit was used to simulate the EIS measurement data of the bare 316L SS substrate, as shown in Figure 9d. Another equivalent circuit was used to simulate the EIS measurement data of the Ta-Nb-N-coated samples, as shown in Figure 9e) The fitting results are given in Table 4. R_s , R_c , and R_p represent solution resistance, charge transfer resistance, and passivation layer resistance, respectively. The constant phase element (CPE) was used to replace the pure capacitance in the circuit, and the impedance was calculated using the following equation:

$$Z_{CPE} = Y_0^{-1}(j\omega)^{-n}, \quad (1)$$

where Y_0 is a parameter, ω the angular frequency, and n is the coefficient [5]. CPE_d is the constant phase element of the double layer, and CPE_p is the constant phase element of the passive layer. R_c is related to the dissolution rate of the metal. The higher the value of R_c , the higher the charge transfer resistance and the better the corrosion resistance. The charge transfer resistance of TaNbN-0.5 coating was approximately $3.8 \times 10^5 \Omega \cdot \text{cm}^2$, which is a significant improvement compared to the charge transfer resistance of approximately $9.73 \times 10^4 \Omega \cdot \text{cm}^2$ of the 316L SS substrate.

Table 4. EIS fitting results of 316L SS and Ta-Nb-N coatings according to the equivalent circuit models.

Samples	$R_s/\Omega \cdot \text{cm}^2$	$CPE_d/\Omega^{-1}\text{cm}^{-2}s^nR_c/\Omega \cdot \text{cm}^2$	n_d	$CPE_p/\Omega^{-1}\text{cm}^{-2}s^n$	n_p	$R_p/\Omega \cdot \text{cm}^2$
316L SS	12.48	5.427×10^{-4}	9728	0.75	1.073×10^{-4}	0.89
TaNbN-0.5	11.79	5.726×10^{-5}	3.844×10^5	0.92	-	-
TaNbN-1.0	8.49	8.747×10^{-5}	1.967×10^5	0.94	-	-
TaNbN-1.5	8.61	9.322×10^{-5}	2.835×10^5	0.91	-	-
TaNbN-2.0	8.304	1.377×10^{-4}	1.678×10^5	0.92	-	-

3.4. ICR and Contact Angle

As shown in Figure 10, the ICR was greatly influenced by the compaction pressure. The higher the compaction force, the greater the effective contact area between the sample and the carbon paper, and the more electron transfer paths. The ICR of 316L SS at 1.4 MPa was approximately $161 \text{ m}\Omega\cdot\text{cm}^2$, which was much higher than the DOE standard [43]. The ICR of 316L SS modified with Ta-Nb-N coatings was significantly reduced. At a pressure of 1.4 MPa, the ICR of the TaNbN-0.5-coated sample was $9.2 \text{ m}\Omega\cdot\text{cm}^2$. Figure 11 compares the corrosion resistance and ICR of this work with those of the previous research [1–3,5–7,9,10,12,14,15,18,20,22,24,26,39–41,44–48]. The use of color has been employed to differentiate the various types of coatings, with C representing carbon-containing coatings, MC metal carbide coatings, MCN metal carbonitride coatings, MN metal nitride coatings, and shape used to differentiate the test environment. The corrosion resistance of Ta-Nb-N coatings prepared in this work is superior to that of most existing reported coatings.

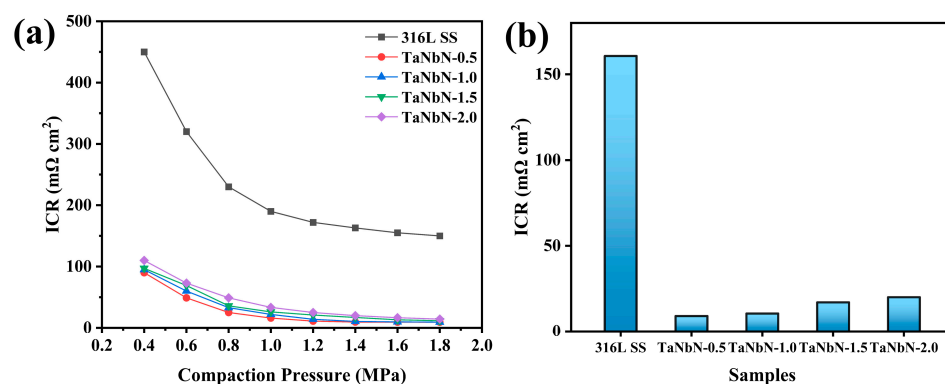


Figure 10. ICR of Ta-Nb-N coatings and 316L SS at different compaction forces (a) and fixed 1.4 MPa (b).

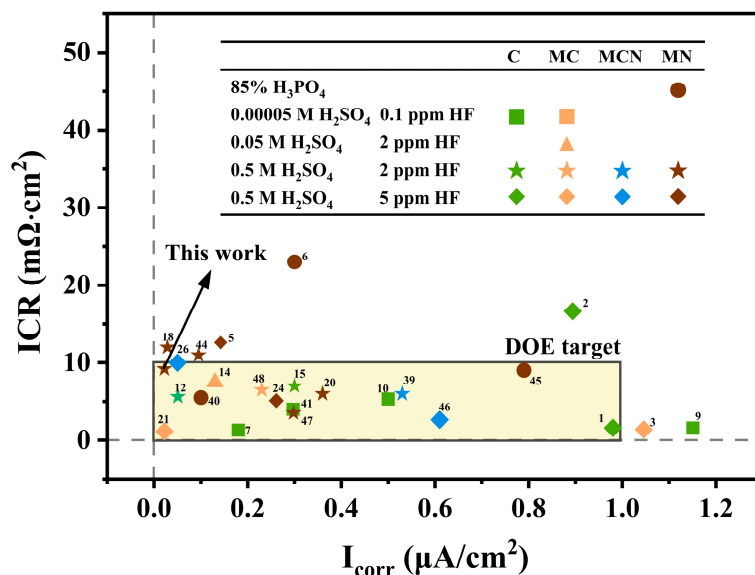


Figure 11. Comparison of corrosion resistance and ICR of this work with previous research.

In the practical operation of PEMFCs, the formation of water is a potential hazard, as its accumulation, if not promptly addressed, leads to obstruction of the gas channel [49]. To ensure efficient water removal, it is essential that the BPs have favorable hydrophobic properties. The water contact angle of 316L SS and the coated sample is 78.5° (316L SS), 100.7° (TaNbN-0.5), 98.2° (TaNbN-1.0), 97.2° (TaNbN-1.5) and 97° (TaNbN-2.0), as shown in Figure 12, implying an improvement in the hydrophobic properties of the metal BPs.

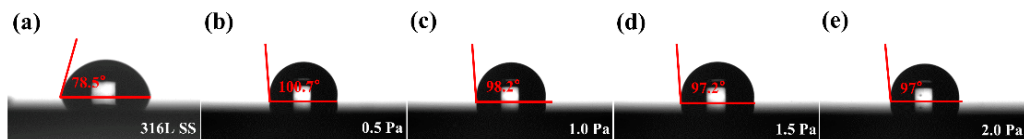


Figure 12. Contact angle of water on (a) 316L SS, (b) TaNbN-0.5, (c) TaNbN-1.0, (d) TaNbN-1.5, and (e) TaNbN-2.0 coatings.

4. Conclusions

The phase composition, micromorphology, corrosion resistance, ICR, and water contact angle of Ta-Nb-N coatings prepared by unbalanced magnetron sputtering at different deposition pressures were investigated. The coatings mostly consist of cubic TaN and cubic NbN, exhibiting dense surface and cross-section structures. The Ta-Nb-N coatings effectively improved the corrosion resistance of 316L SS. The corrosion current density of Ta-Nb-N-coated BPs was reduced to $2.2 \times 10^{-2} \mu\text{A}\cdot\text{cm}^{-2}$ in a corrosion electrolyte ($0.5 \text{ M H}_2\text{SO}_4 + 2 \text{ ppm HF}$ at 70°C) harsher than the DOE. In the potentiostatic test, the corrosion current density of each coating decreased steadily, indicating that the coating has high corrosion resistance. The EIS test also showed that the coatings have high charge transfer resistance and inhibit corrosion. In addition, the ICR of the TaNbN-0.5 coating was $9.2 \text{ m}\Omega\cdot\text{cm}^2$, which meets the DOE 2025 standard. The results indicate that Ta-Nb-N coatings could be a suitable material for BPs.

Supplementary Materials: The following supporting information can be downloaded at <https://www.mdpi.com/article/10.3390/coatings14050542/s1>. Figure S1: Diagram of the electrochemical test device; Figure S2: (a) Schematic illustration of the technique used for the ICR test. (b) Partial enlargement of the device.

Author Contributions: Conceptualization, R.T. and Q.L.; methodology, C.D.; software, T.G. (Takashi Goto); validation, M.Y. (Mai Yang); formal analysis, R.T. and C.D.; investigation, M.Y. (Meijun Yang); resources, S.Z.; data curation, R.T.; writing—original draft preparation, C.D., Q.L., and R.T.; writing—review and editing, R.T.; visualization, B.J.; supervision, T.G. (Tenghua Gao); project administration, S.Z.; funding acquisition, R.T. All authors have read and agreed to the published version of the manuscript.

Funding: This work was supported by the Guangdong Major Project of Basic and Applied Basic Research (2021B0301030001), the Self-Innovation Research Funding Project of Hanjiang Laboratory (HJL202012A002, HJL202012A003), and the Major Science and Technology Project in Zhongshan City, Guangdong Province (2019AG029). This work was also supported by the National Natural Science Foundation of China (Nos. 51972244, 52002075, and 62204179) and the 111 Project (B13035). It was further supported by the International Science & Technology Cooperation Program of China (2018YFE0103600) and the Technological Innovation of Hubei Province (2019AAA030), China.

Institutional Review Board Statement: Not applicable.

Informed Consent Statement: Not applicable.

Data Availability Statement: Data are contained within the article.

Conflicts of Interest: The authors declare that they have no known competing financial interests or personal relationships that could have appeared to influence the work reported in this paper.

References

- Yan, W.; Zhang, Y.; Chen, L.; Luo, J.; Pang, P.; Zhang, X.; Liao, B.; Ying, M. Corrosion behavior and interfacial conductivity of amorphous hydrogenated carbon and titanium carbide composite (a-C: H/TiC) films prepared on titanium bipolar plates in PEMFCs. *Diam. Relat. Mater.* **2021**, *120*, 108628–108637. [[CrossRef](#)]
- Mingge, W.; Congda, L.; Tao, H.; Guohai, C.; Donghui, W.; Haifeng, Z.; Dong, Z.; Aiying, W. Chromium interlayer amorphous carbon film for 304 stainless steel bipolar plate of proton exchange membrane fuel cell. *Surf. Coat. Technol.* **2016**, *307*, 374–381. [[CrossRef](#)]
- Zhao, Y.; Wei, L.; Yi, P.; Peng, L. Influence of Cr-C film composition on electrical and corrosion properties of 316L stainless steel as bipolar plates for PEMFCs. *Int. J. Hydrog. Energy* **2016**, *41*, 1142–1150. [[CrossRef](#)]

4. Wang, X.-Z.; Muneshwar, T.P.; Fan, H.-Q.; Cadien, K.; Luo, J.-L. Achieving ultrahigh corrosion resistance and conductive zirconium oxynitride coating on metal bipolar plates by plasma enhanced atomic layer deposition. *J. Power Sources* **2018**, *397*, 32–36. [[CrossRef](#)]
5. Jin, J.; He, Z.; Zhao, X. Effect of Al content on the corrosion resistance and conductivity of metal nitride coating in the cathode environment of PEMFCs. *Mater. Chem. Phys.* **2020**, *245*, 122739. [[CrossRef](#)]
6. Lee, S.H.; Kakati, N.; Maiti, J.; Jee, S.H.; Kalita, D.J.; Yoon, Y.S. Corrosion and electrical properties of CrN- and TiN-coated 316L stainless steel used as bipolar plates for polymer electrolyte membrane fuel cells. *Thin Solid Film.* **2013**, *529*, 374–379. [[CrossRef](#)]
7. Yi, P.; Zhang, W.; Bi, F.; Peng, L.; Lai, X. Microstructure and properties of a-C films deposited under different argon flow rate on stainless steel bipolar plates for proton exchange membrane fuel cells. *J. Power Sources* **2019**, *410–411*, 188–195. [[CrossRef](#)]
8. Asri, N.F.; Husaini, T.; Sulong, A.B.; Majlan, E.H.; Daud, W.R.W. Coating of stainless steel and titanium bipolar plates for anticorrosion in PEMFC: A review. *Int. J. Hydrot. Energy* **2017**, *42*, 9135–9148. [[CrossRef](#)]
9. Zhang, D.; Yi, P.; Peng, L.; Lai, X.; Pu, J. Amorphous carbon films doped with silver and chromium to achieve ultra-low interfacial electrical resistance and long-term durability in the application of proton exchange membrane fuel cells. *Carbon* **2019**, *145*, 333–344. [[CrossRef](#)]
10. Yi, P.; Zhang, D.; Peng, L.; Lai, X. Impact of Film Thickness on Defects and the Graphitization of Nanothin Carbon Coatings Used for Metallic Bipolar Plates in Proton Exchange Membrane Fuel Cells. *ACS Appl. Mater. Interfaces* **2018**, *10*, 34561–34572. [[CrossRef](#)] [[PubMed](#)]
11. Suherman, H.; Sulong, A.B.; Sahari, J. Effect of the compression molding parameters on the in-plane and through-plane conductivity of carbon nanotubes/graphite/epoxy nanocomposites as bipolar plate material for a polymer electrolyte membrane fuel cell. *Ceram. Int.* **2013**, *39*, 1277–1284. [[CrossRef](#)]
12. Li, W.; Liu, L.-T.; Li, Z.-X.; Wang, Y.-F.; Li, H.-Z.; Lei, J.-J. Corrosion resistance and conductivity of amorphous carbon coated SS316L and TA2 bipolar plates in proton-exchange membrane fuel cells. *Diam. Relat. Mater.* **2021**, *118*, 108503. [[CrossRef](#)]
13. Wang, L.; Sun, J.; Sun, J.; Lv, Y.; Li, S.; Ji, S.; Wen, Z. Niobium nitride modified AISI 304 stainless steel bipolar plate for proton exchange membrane fuel cell. *J. Power Sources* **2012**, *199*, 195–200. [[CrossRef](#)]
14. Shi, J.; Zhang, P.; Han, Y.; Wang, H.; Wang, X.; Yu, Y.; Sun, J. Investigation on electrochemical behavior and surface conductivity of titanium carbide modified Ti bipolar plate of PEMFC. *Int. J. Hydrot. Energy* **2020**, *45*, 10050–10058. [[CrossRef](#)]
15. Show, Y.; Miki, M.; Nakamura, T. Increased in output power from fuel cell used metal bipolar plate coated with a-C film. *Diam. Relat. Mater.* **2007**, *16*, 1159–1161. [[CrossRef](#)]
16. Yi, P.; Zhang, D.; Qiu, D.; Peng, L.; Lai, X. Carbon-based coatings for metallic bipolar plates used in proton exchange membrane fuel cells. *Int. J. Hydrot. Energy* **2019**, *44*, 6813–6843. [[CrossRef](#)]
17. Yu, H.; Yang, L.; Zhu, L.; Jian, X.; Wang, Z.; Jiang, L. Anticorrosion properties of Ta-coated 316L stainless steel as bipolar plate material in proton exchange membrane fuel cells. *J. Power Sources* **2009**, *191*, 495–500. [[CrossRef](#)]
18. Alishahi, M.; Mahboubi, F.; Mousavi Khoie, S.M.; Aparicio, M.; Hübler, R.; Soldner, F.; Gago, R. Electrochemical behavior of nanocrystalline Ta/TaN multilayer on 316L stainless steel: Novel bipolar plates for proton exchange membrane fuel-cells. *J. Power Sources* **2016**, *322*, 1–9. [[CrossRef](#)]
19. Choe, C.; Choi, H.; Hong, W.; Lee, J.-J. Tantalum nitride coated AISI 316L as bipolar plate for polymer electrolyte membrane fuel cell. *Int. J. Hydrot. Energy* **2012**, *37*, 405–411. [[CrossRef](#)]
20. Tu, R.; Min, R.; Yang, M.; Yuan, Y.; Zheng, L.; Li, Q.; Ji, B.; Zhang, S.; Yang, M.; Shi, J. Overcoming the Dilemma between Low Electrical Resistance and High Corrosion Resistance Using a Ta/(Ta,Ti)N/TiN/Ti Multilayer for Proton Exchange Membrane Fuel Cells. *Coatings* **2022**, *12*, 689–704. [[CrossRef](#)]
21. Gou, Y.; Chen, H.; Li, R.; Geng, J.; Shao, Z. Nb–Cr–C coated titanium as bipolar plates for proton exchange membrane fuel cells. *J. Power Sources* **2022**, *520*, 230797–230805. [[CrossRef](#)]
22. Hu, Q.; Gao, J.-Y.; Shu, S.; Xu, Y.-X.; Luo, J.-L.; Wang, X.-Z. Corrosion behaviors of multilayer C/Cr/SS bipolar plates for proton exchange membrane fuel cells under dynamic potential polarization based on New European Driving Cycle. *Corros. Sci.* **2023**, *214*, 111032. [[CrossRef](#)]
23. Zhao, T.; Shen, S.; Liu, X.; Guo, Y.; Pao, C.-W.; Chen, J.-L.; Wang, Y. Morphology-maintaining synthesis of NbN and its catalytic performance in epoxidation. *Catal. Sci. Technol.* **2019**, *9*, 4002–4009. [[CrossRef](#)]
24. Bi, F.; Yi, P.; Zhou, T.; Peng, L.; Lai, X. Effects of Al incorporation on the interfacial conductivity and corrosion resistance of CrN film on SS316L as bipolar plates for proton exchange membrane fuel cells. *Int. J. Hydrot. Energy* **2015**, *40*, 9790–9802. [[CrossRef](#)]
25. Peng, S.; Xu, J.; Li, Z.; Jiang, S.; Munroe, P.; Xie, Z.-H.; Lu, H. A reactive-sputter-deposited TiSiN nanocomposite coating for the protection of metallic bipolar plates in proton exchange membrane fuel cells. *Ceram. Int.* **2020**, *46*, 2743–2757. [[CrossRef](#)]
26. Jin, J.; Zhang, J.; Hu, M.; Li, X. Investigation of high potential corrosion protection with titanium carbonitride coating on 316L stainless steel bipolar plates. *Corros. Sci.* **2021**, *191*, 109757. [[CrossRef](#)]
27. Gou, Y.; Jiang, G.; Hao, J.; Shao, Z.; Wei, Z. A corrosion mechanism of NbC/α-C:H films for metallic bipolar plates in proton exchange membrane fuel cell cathode based on percolation model. *Surf. Coat. Technol.* **2022**, *445*, 128711. [[CrossRef](#)]
28. Shen, H.; Wang, L. Characterization and properties of NbN–Nb bilayer formed on titanium for bipolar plates. *Mater. Chem. Phys.* **2022**, *290*, 126628–126636. [[CrossRef](#)]
29. Jin, J.; Hu, M.; Zhao, X. Investigation of incorporating oxygen into TiN coating to resist high potential effects on PEMFC bipolar plates in vehicle applications. *Int. J. Hydrot. Energy* **2020**, *45*, 23310–23326. [[CrossRef](#)]

30. Wang, H. Stainless steel as bipolar plate material for polymer electrolyte membrane fuel cells. *J. Power Sources* **2003**, *115*, 243–251. [[CrossRef](#)]
31. Tang, Y.; Yuan, W.; Pan, M.; Wan, Z. Feasibility study of porous copper fiber sintered felt: A novel porous flow field in proton exchange membrane fuel cells. *Int. J. Hydrol. Energy* **2010**, *35*, 9661–9677. [[CrossRef](#)]
32. Chen, M.; Ding, J.C.; Kwon, S.-H.; Wang, Q.; Zhang, S. Corrosion resistance and conductivity of NbN-coated 316L stainless steel bipolar plates for proton exchange membrane fuel cells. *Corros. Sci.* **2022**, *196*, 110042–110052. [[CrossRef](#)]
33. Lamour, P.; Fioux, P.; Ponche, A.; Nardin, M.; Vallat, M.F.; Dugay, P.; Brun, J.P.; Moreaud, N.; Pinvidic, J.M. Direct measurement of the nitrogen content by XPS in self-passivated TaNx thin films. *Surf. Interface Anal.* **2008**, *40*, 1430–1437. [[CrossRef](#)]
34. Kościelska, B.; Winiarski, A. Structural investigations of nitrided Nb_2O_5 and $\text{Nb}_2\text{O}_5\text{-SiO}_2$ sol–gel derived films. *J. Non-Cryst. Solids* **2008**, *354*, 4349–4353. [[CrossRef](#)]
35. Chen, J.; Zhang, S.; Zheng, J.; Dong, Y.; Zhang, C.; Li, J.; Chen, Z.; Zhang, J.; Sun, D. Excellent anti-corrosion and conductivity of NbN coated on Ti bipolar plate by controlling N2 flow rates. *J. Alloys Compd.* **2024**, *976*, 173033. [[CrossRef](#)]
36. Jeong, J.J.; Lee, C.M. Effects of post-deposition annealing on the mechanical and chemical properties of the $\text{Si}_3\text{N}_4/\text{NbN}$ multilayer coatings. *Appl. Surf. Sci.* **2003**, *214*, 11–19. [[CrossRef](#)]
37. Ufuktepe, Y.; Farha, A.H.; Kimura, S.I.; Hajiri, T.; Imura, K.; Mamun, M.A.; Karadag, F.; Elmustafa, A.A.; Elsayed-Ali, H.E. Superconducting niobium nitride thin films by reactive pulsed laser deposition. *Thin Solid Film.* **2013**, *545*, 601–607. [[CrossRef](#)]
38. Ingle, A.V.; Raja, V.S.; Rangarajan, J.; Mishra, P. Corrosion resistant quaternary Al–Cr–Mo–N coating on type 316L stainless steel bipolar plates for proton exchange membrane fuel cells. *Int. J. Hydrol. Energy* **2020**, *45*, 3094–3107. [[CrossRef](#)]
39. Pan, T.J.; Dai, Y.J.; Jiang, J.; Xiang, J.H.; Yang, Q.Q.; Li, Y.S. Anti-corrosion performance of the conductive bilayer CrC/CrN coated 304SS bipolar plate in acidic environment. *Corros. Sci.* **2022**, *206*, 110495–110506. [[CrossRef](#)]
40. Li, R.; Cai, Y.; Wippermann, K.; Lehnert, W. Bilayer CrN/Cr coating-modified 316L stainless steel bipolar plates for high temperature polymer electrolyte fuel cells. *J. Power Sources* **2019**, *434*, 226718–226725. [[CrossRef](#)]
41. Zhang, W.; Yi, P.; Peng, L.; Lai, X. Strategy of alternating bias voltage on corrosion resistance and interfacial conductivity enhancement of $\text{TiCx}/\text{a-C}$ coatings on metallic bipolar plates in PEMFCs. *Energy* **2018**, *162*, 933–943. [[CrossRef](#)]
42. Wang, X.-H.; Wang, J.-H.; Fu, C.-W. Characterization of pitting corrosion of 7A60 aluminum alloy by EN and EIS techniques. *Trans. Nonferrous Met. Soc. China* **2014**, *24*, 3907–3916. [[CrossRef](#)]
43. Yan, P.; Ying, T.; Yang, Y.; Cao, F.; Li, Y.; Wang, J.; Zeng, X. Investigation of anodized Ta/Ag coating on magnesium bipolar plate for lightweight proton exchange membrane fuel cells. *Corros. Sci.* **2022**, *197*, 110086. [[CrossRef](#)]
44. Wang, L.; Tao, Y.; Zhang, Z.; Wang, Y.; Feng, Q.; Wang, H.; Li, H. Molybdenum carbide coated 316L stainless steel for bipolar plates of proton exchange membrane fuel cells. *Int. J. Hydrol. Energy* **2019**, *44*, 4940–4950. [[CrossRef](#)]
45. Jannat, S.; Rashtchi, H.; Atapour, M.; Golozar, M.A.; Elmkhah, H.; Zhiani, M. Preparation and performance of nanometric Ti/TiN multi-layer physical vapor deposited coating on 316L stainless steel as bipolar plate for proton exchange membrane fuel cells. *J. Power Sources* **2019**, *435*, 226818. [[CrossRef](#)]
46. Wang, L.; Li, L.; Liu, H.; Wang, S.; Fang, H.; Gao, H.; Gao, K.; Zhang, Y.; Sun, J.; Yan, J. Polylaminate TaN/Ta coating modified ferritic stainless steel bipolar plate for high temperature proton exchange membrane fuel cell. *J. Power Sources* **2018**, *399*, 343–349. [[CrossRef](#)]
47. Yi, P.; Peng, L.; Zhou, T.; Wu, H.; Lai, X. Cr–N–C multilayer film on 316L stainless steel as bipolar plates for proton exchange membrane fuel cells using closed field unbalanced magnetron sputter ion plating. *Int. J. Hydrol. Energy* **2013**, *38*, 1535–1543. [[CrossRef](#)]
48. Wang, Z.; Zhang, B.; Gao, K.; Liu, R. Adjustable TiN coatings deposited with HiPIMS on titanium bipolar plates for PEMFC. *Int. J. Hydrol. Energy* **2022**, *47*, 39215–39224. [[CrossRef](#)]
49. Wang, L.; Sun, J.; Li, P.; Jing, B.; Li, S.; Wen, Z.; Ji, S. Niobized AISI 304 stainless steel bipolar plate for proton exchange membrane fuel cell. *J. Power Sources* **2012**, *208*, 397–403. [[CrossRef](#)]

Disclaimer/Publisher’s Note: The statements, opinions and data contained in all publications are solely those of the individual author(s) and contributor(s) and not of MDPI and/or the editor(s). MDPI and/or the editor(s) disclaim responsibility for any injury to people or property resulting from any ideas, methods, instructions or products referred to in the content.